Lawrence Berkeley National Laboratory
Recent Work

Title
Subterahertz collective dynamics of polar vortices.

Permalink
https://escholarship.org/uc/item/6r31x9v0

Journal
Nature, 592(7854)

ISSN
0028-0836

Authors
Li, Qian
Stoica, Vladimir A
Paściak, Marek
et al.

Publication Date
2021-04-01

DOI
10.1038/s41586-021-03342-4

Peer reviewed

Article

Subterahertz collective dynamics of polar vortices

Qian Li[1,11,13], Vladimir A. Stoica[1,2,13], Marek Paściak[3], Yi Zhu[1], Yakun Yuan[2], Tiannan Yang[2], Margaret R. McCarter[4], Sujit Das[4], Ajay K. Yadav[4], Suji Park[7,12], Cheng Dai[2], Hyeon Jun Lee[8], Youngjun Ahn[8], Samuel D. Marks[8], Shukai Yu[2], Christelle Kadlec[3], Takahiro Sato[9], Matthias C. Hoffmann[9], Matthieu Chollet[9], Michael E. Kozina[9], Silke Nelson[9], Diling Zhu[9], Donald A. Walko[1], Aaron M. Lindenberg[7,10], Paul G. Evans[8], Long-Qing Chen[2], Ramamoorthy Ramesh[4,5,6], Lane W. Martin[4,6], Venkatraman Gopalan[2], John W. Freeland[1], Jirka Hlinka[3] & Haidan Wen[1✉]

The collective dynamics of topological structures[1–6] are of interest from both fundamental and applied perspectives. For example, studies of dynamical properties of magnetic vortices and skyrmions[3,4] have not only deepened our understanding of many-body physics but also offered potential applications in data processing and storage[7]. Topological structures constructed from electrical polarization, rather than electron spin, have recently been realized in ferroelectric superlattices[5,6], and these are promising for ultrafast electric-field control of topological orders. However, little is known about the dynamics underlying the functionality of such complex extended nanostructures. Here, using terahertz-field excitation and femtosecond X-ray diffraction measurements, we observe ultrafast collective polarization dynamics that are unique to polar vortices, with orders-of-magnitude higher frequencies and smaller lateral size than those of experimentally realized magnetic vortices[3]. A previously unseen tunable mode, hereafter referred to as a vortexon, emerges in the form of transient arrays of nanoscale circular patterns of atomic displacements, which reverse their vorticity on picosecond timescales. Its frequency is considerably reduced (softened) at a critical strain, indicating a condensation (freezing) of structural dynamics. We use first-principles-based atomistic calculations and phase-field modelling to reveal the microscopic atomic arrangements and corroborate the frequencies of the vortex modes. The discovery of subterahertz collective dynamics in polar vortices opens opportunities for electric-field-driven data processing in topological structures with ultrahigh speed and density.

Precisely engineered $(PbTiO_3)_n/(SrTiO_3)_n$ oxide superlattices provide a controllable material that can host new phenomena such as negative capacitance[8,9] and light-induced supercrystals[10], as well as unique polarization topologies including vortex[5] and skyrmion[6] structures. Unlike their counterparts in magnetic systems[3,4,11], the building elements of these extended nanostructures are electric polarizations and thus may have collective dynamics and properties that do not exist in magnetic systems: the direct interaction of polarization with electric fields allows electric-field excitation of their dynamics on ultrafast timescales, and the intrinsic coupling of polarization with the lattice offers strain tunability. These advantages have motivated research into ferroelectric (FE) materials for next-generation electronics. For example,

nanoscale FE domain walls have been envisaged for ultrahigh-speed microelectronics and telecommunications[12–16] and host collective dynamics at terahertz (THz) frequencies[17–20], whereas magnetic vortices and skyrmions typically have dynamics in the few gigahertz range[7,21]. However, such THz dynamics in topological polar structures have not been experimentally demonstrated.

Collective dynamics also hold the key to understanding many-body interactions in these newly discovered topological polar structures where long-range interactions beyond the nearest neighbours are crucial[22]. The dynamics of 'soft modes' that exhibit a reduction of the mode frequency toward a critical point are important to understanding the thermodynamics of phase transitions[23], gaining access to hidden

[1]Advanced Photon Source, Argonne National Laboratory, Lemont, IL, USA. [2]Department of Materials Science and Engineering, The Pennsylvania State University, University Park, PA, USA. [3]Institute of Physics of the Czech Academy of Sciences, Prague, Czech Republic. [4]Department of Materials Science and Engineering, University of California, Berkeley, Berkeley, CA, USA. [5]Department of Physics, University of California, Berkeley, Berkeley, CA, USA. [6]Materials Sciences Division, Lawrence Berkeley National Laboratory, Berkeley, CA, USA. [7]SIMES, SLAC National Accelerator Laboratory, Menlo Park, CA, USA. [8]Department of Materials Science and Engineering, University of Wisconsin-Madison, Madison, WI, USA. [9]Linac Coherent Light Source, SLAC National Accelerator Laboratory, Menlo Park, CA, USA. [10]Department of Materials Science and Engineering, Stanford University, Stanford, CA, USA. [11]School of Materials Science and Engineering, Tsinghua University, Beijing, China. [12]Present address: Center for Functional Nanomaterials, Brookhaven National Laboratory, Upton, NY, USA. [13]These authors contributed equally: Qian Li, Vladimir A. Stoica. ✉e-mail: wen@anl.gov

ferroelectricity far from equilibrium[24], and condensing metastable polar phases[25]. However, whether topological structures host new soft modes and how they behave on ultrafast timescales are unanswered questions for elucidating the fundamental physics and exploring the properties of these emergent nanostructures.

We focus our study on polar vortices[5], a prototypical topological structure of nanoscale FE materials. The unique connectivity of electric polarization (**P**) that continuously rotates around a core with non-zero curl ($\nabla \times \mathbf{P}$) in each vortex supercell can give rise to a series of new collective modes. Response spectra computed by dynamical phase-field modelling show a series of modes consistent with what we experimentally observe in the vortex structure (orange arrows, Fig. 1a). These modes are distinct from optical phonons in bulk ferroelectrics[23], acoustic modes in superlattices[26] and chiral phonons in a hexagonal lattice[27]. Besides high-frequency modes in the range 0.3–0.4 THz, we identified a low-frequency vortexon mode with a characteristic frequency ω ('V' mode, Fig. 1a) tunable by thermally induced strain in the low-frequency regime. The atomistic simulations show that this mode emerges as a transient nanoscale circular pattern of collective atomic motion (purple circles, Fig. 1b). Its time-dependent vorticity ($\nabla \times \mathbf{u}$) of atomic displacements **u** oscillates on picosecond timescales, interweaving with polar vortices (magenta circles). A zoom-in snapshot shows the nanoscale collective circular patterns spanning many unit cells with a lateral size of ~6 nm, much smaller than the typical submicrometre size of magnetic vortices.

Observations of collective modes

Measurements made with the THz pump and hard X-ray diffraction probe technique at the Linac Coherent Light Source (Fig. 1c and Methods) revealed these collective modes in 100-nm-thick $(PbTiO_3)_{16}/(SrTiO_3)_{16}$ superlattices grown on $DyScO_3$ (DSO) substrates. This technique circumvents the challenges of detecting incoherent modes in heterogeneous systems because the coherent THz field acts as an impulsive excitation to synchronize the polarization dynamics[28–31] and the X-ray diffraction selectively probes the vortex and conventional ferroelectric (FE) a_1/a_2-domain structures[32]. These vortex and FE structures coexist in the sample (Methods), but their diffraction signals can be probed separately in reciprocal space due to distinct lattice parameters (Fig. 2a and Extended Data Fig. 1a). The polarization direction of the applied THz field with respect to the crystalline axes was determined by the diffraction geometry and sample orientation (Extended Data Fig. 1b).

The structural response of the polar vortices upon THz excitation can be categorized into two frequency regimes. The high-frequency regime features multiple modes in the range 0.3–0.4 THz, observed by probing selected Bragg peaks (Fig. 2a). For example, the diffraction intensities of the 023 peak and its satellites were modulated at the same frequency but with opposite phases (Fig. 2b). This indicated that the weakening or enhancement of the in-plane vortex order redistributed the diffraction intensity from the satellites to the main peak or vice versa. The THz field directly excited the superlattice layer rather than the substrate, since there was no measurable structural response of the latter. The Fourier analysis of the intensity oscillations revealed that the frequency components peaked at 0.34 THz and 0.38 THz (orange arrows in Fig. 2c). To simultaneously capture the response of the conventional FE domain structure, we monitored the 113 reflections of both the FE superlattice peak and the vortex satellites with identical excitation conditions (Fig. 2b). The FE domain structure[32] exhibited a spectral fingerprint at 0.22 THz (blue arrow in Fig. 2c and Extended Data Fig. 2), in analogy to the previously predicted inhomogeneous phason mode[18]. Its frequency is different from that of the vortex structure, suggesting that the collective dynamics of FE and vortex structures are uniquely associated with their microscopic polarization configurations. The diffraction signals monitored across the 023 FE Bragg
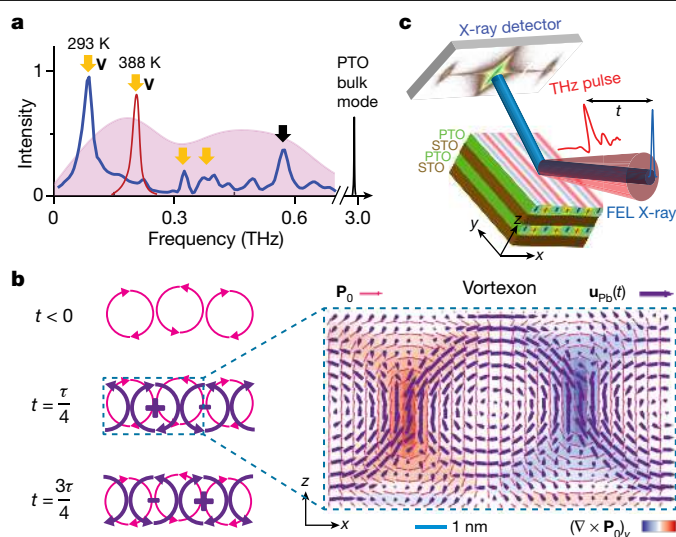

Fig. 1 | Emergence of the collective dynamics of polar vortices and its experimental detection. a, Fourier spectra (blue) of calculated time-dependent response of polar vortices on THz-field excitation. The spectrum of the THz pulse is shown as a broad pink background. The collective modes of polar vortices (orange arrows) are shown as a separate set of modes with respect to the known superlattice acoustic modes (black arrow) and the soft mode of PbTiO_3 at room temperature. The vortexon mode (V) shifts to higher frequency (red peak; note that this is not the calculated peak but a schematic peak to show the temperature dependence) as sample temperature increases. **b**, Emergence and evolution of the vortexon (atomic displacement vortices, purple circles) during its oscillation period τ, overlaid with the static polarization vortices (magenta circles). + and −, the signs of vortexon vorticity, which reverse dynamically. Right, zoomed-in view of the region of the dashed box with the calculated static polarization (magenta arrows) and lead-cation displacement (purple arrows) in each unit cell of the vortexon mode at $t = \tau/4$. **c**, Schematic of THz-pump and X-ray-diffraction-probe experiment using an X-ray free-electron laser (FEL). The coloured stripes on the $(PbTiO_3)_{16}/(SrTiO_3)_{16}$ (PTO/STO) superlattice film represent in-plane vortex orders with opposite polarization vorticity.

peak oscillated in phase (Extended Data Fig. 2c, d), showing that the Bragg peak was modulated in overall peak intensity as the structure factor of the FE domain changed, rather than the peak shifting or broadening. The magnitude of the effects was proportional to the peak THz field, in agreement with a field-driven mechanism rather than a parabolic dependence due to THz-induced heating (Extended Data Fig. 2b).

Complementary microscopic pictures of the collective modes were obtained through atomistic and dynamical phase-field modelling (Methods and Supplementary Notes 1 and 2), with the former seeking the equilibrium eigenmodes based on first-principles-derived ionic potentials[18] and the latter addressing the driven dynamics of the polarization order parameter[33,34]. The atomistic model revealed multiple prominent eigenmodes in the same high-frequency regime (Extended Data Fig. 3). Microscopic dynamical properties are illustrated using the calculated 0.30-THz mode as an example because its calculated dielectric response is relatively large and likely to be observed. Snapshots of its polarization vectors are shown at the equilibrium state ($t < 0$) and the maximum ($t = \tau/4$) of the atomic displacement during a sinusoidal oscillation (Fig. 2d and Supplementary Video 1). In this mode, the central positions of the polar vortices do not change along the z-axis, and the dominant lead-cation displacement is along the x-axis (Fig. 2e). To illustrate the diversity of the dynamics in this frequency range, complex configurations of polarizations and atomic displacements of additional modes are shown in Extended Data Fig. 4. Their infrared activity corresponds well with the observed THz absorption (Supplementary Note 7).
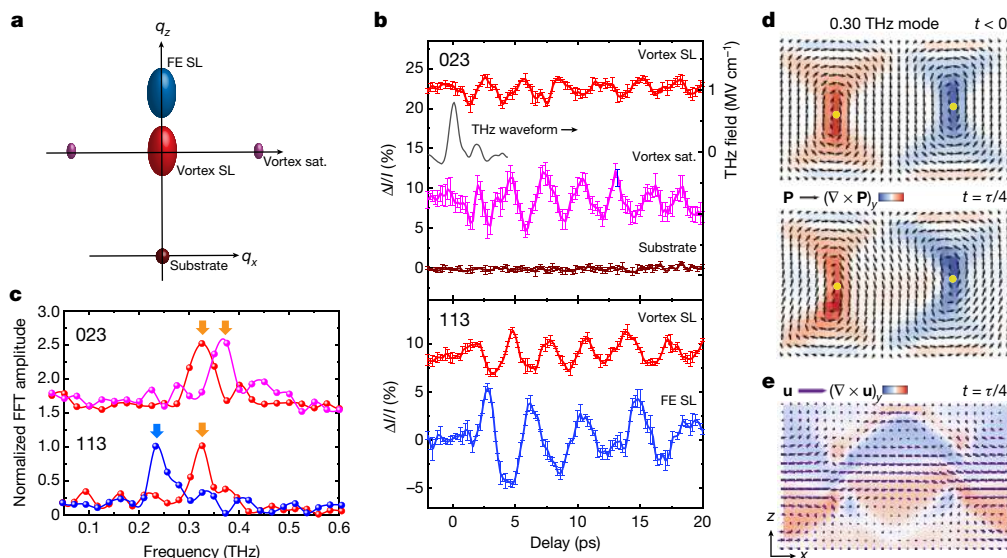
Fig. 2 | High-frequency collective modes. a, Schematic of the probed Bragg peaks in the q_x–q_z plane of the reciprocal space around the 023, 113 and 004 substrate peaks. FE, ferroelectric a_1/a_2 structure; sat., satellite peak; SL, superlattice peak; substrate, DSO peak. **b**, Normalized change of diffraction intensity of the Bragg peaks (indicated by the same colour scheme as in **a**) as a function of delay, with the measured THz excitation pulse overlaid (THz waveform scale indicated on the right). The error bars show the standard errors. **c**, The corresponding Fourier spectra with marked vortex modes (orange arrows) and FE modes (blue arrow). The curves in **b** and **c** are offset vertically for clarity. FFT, fast Fourier transform. **d**, Polarization (**P**) of a calculated 0.30-THz vortex mode at the equilibrium state ($t < 0$) and the sinusoidal maximum ($t = \tau/4$), with associated vorticity (colour). **e**, Lead-cation displacements (**u**) and associated vorticity (colour) at $t = \tau/4$. The structural distortion is enhanced for better visibility.

The low-frequency regime features the vortexon mode at 0.08 THz at room temperature, which was observed from the diffraction intensity change of the 004-vortex peak (Fig. 3a). Remarkably, this unique mode was highly sensitive to temperature. An increase in sample temperature from 293 K to 388 K resulted in hardening of this mode from 0.08 THz to 0.23 THz (Fig. 3a, b), in contrast to any known modes in bulk or strained $PbTiO_3$ and $SrTiO_3$. The amplitude of the oscillation decreased as the sample temperature increased, which correlated well with the

weakening of the vortex order[32]. The intensities of the $\delta 04$-satellite peaks with a small in-plane scattering component, $\delta = \pm 0.059\,\text{Å}^{-1}$, exhibit strong high-frequency oscillations at 0.34 THz and 0.38 THz, consistent with the measurements of the 023 and 113 peaks. However, these frequencies did not change as a function of temperature. At higher temperatures, closer to the vortex-ordering temperature of 473 K (ref. [32]), the vortex order was further reduced so that the X-ray diffraction intensity was too weak to measure. The oscillation amplitudes of all
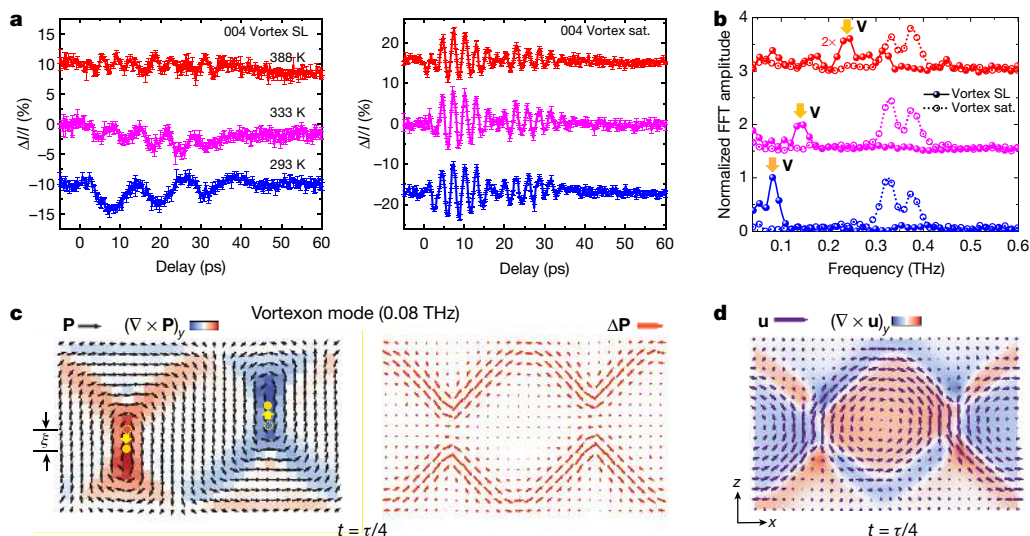

Fig. 3 | Tunable vortexon mode. a, Normalized change of diffraction intensity of 004-superlattice (SL) and $\delta 04$-satellite peaks of vortex structures as a function of delay at various temperatures. The error bars show the standard errors. **b**, Corresponding Fourier spectra of the intensity oscillations of the 004 SL peak (solid) and $\delta 04$-satellite peaks (open circles), normalized to the spectra at 293 K. The orange arrows indicate the tunable vortexon mode. The curves in **a** and **b** are offset vertically for clarity. FFT, fast Fourier transform.

c, Calculated polarization (**P**) and change of polarization (Δ**P**) of the vortexon at the sinusoidal maximum ($t = \tau/4$). The yellow arrows indicate the shift of vortex cores (solid dots) from the equilibrium positions (open yellow circles) by a distance ξ compared with the case of $t < 0$ shown in Fig. 2d. **d**, Lead-cation displacements (**u**) and associated vorticity (colour) at $t = \tau/4$. The vector lengths of **u** and the shift ξ are enlarged (arbitrarily and by 2.5 times, respectively) for better visibility.

modes were reduced after 36 ps, which was the time for the completion of lattice expansion (Extended Data Fig. 2g, h). Possible causes for this amplitude reduction may be related to the leakage of the mechanical energy into the substrate[35].

The observation of the 0.08-THz mode in the vortex structure is corroborated by a low-frequency mode which is well separated from high-frequency ones in the atomistic model. Examining its polarization dynamics, we found that the centres of a pair of polar vortices shift in opposite directions along the z-axis (Fig. 3c, Supplementary Video 2), unlike magnetic vortex cores, which have a gyratory motion[3]. The polarization change ΔP forms a wavy structure as a result of collective motions of lead, titanium and oxygen atoms. The corresponding lead-cation displacements are linear within the unit cell, in contrast to the circular atomic motion of chiral phonons[27,36]. They collectively form a circular pattern, producing a transient non-zero curl of atomic displacement $\nabla \times \mathbf{u}(t)$ (Fig. 3d), hence the name vortexon. This circular pattern of atomic displacement gives rise to a transient angular momentum with respect to the vortexon cores (Supplementary Note 1B). Titanium and oxygen ionic motions follow similar patterns (Extended Data Fig. 4). The maximum displacement occurs at locations with a large curl of polarization, suggesting that the pre-existing polarization gradient within the supercell facilitates the structural response to the THz field. As a result, the vortexon cores (centres of purple circles in Fig. 1b) are spatially shifted by half a period with respect to the core of the equilibrium polar-vortex structure (centres of magenta circles in Fig. 1b). The orientation of the THz field with respect to the crystalline axes can influence the amplitude but not the frequency of this mode. Experimentally, when the THz field is aligned perpendicular to the x-axis, the vortex response is stronger than when the THz field is parallel to the x-axis (Extended Data Fig. 5a, Supplementary Note 5), which is different from the prediction by the simplified models (Supplementary Note 6).

Discussion

We identified the dominant role of thermally induced strain in producing the observed large tunability of the vortexon mode. The variation of the strain due to a temperature rise of 95 K, confirmed by X-ray diffraction measurements (Extended Data Fig. 7a, b), amounts to a lattice expansion of 0.1% along the x-axis. We then theoretically explored the effect of strain (ε) on the eigenmodes. The zero strain was defined specifically in the atomistic and phase-field models (Supplementary Notes 1 and 2). These two independent theoretical approaches produced the same trends (Fig. 4a). Numerous modes lying in the range 0.3–0.4 THz were insensitive to strain variation, whereas a distinct low-frequency mode can be effectively tuned by strain, in agreement with observed in-plane strain variations in the range of −0.1% to 0.04% due to the temperature changes from 293 K to 388 K. The softening of the frequency towards a critical strain ε_c (−0.3% in the atomistic model and −0.2% in the phase-field simulation) is phenomenologically similar to phonon softening close to a structural phase transition. Indeed, the atomistic models show that the polar vortices go through a symmetry-breaking transition from symmetric to staggered vortex-core pairs (Fig. 4a, bottom inset) across the critical strain, different from a temperature-induced order–disorder vortex phase transition[32]. The equilibrium state consists of the staggered vortices in which the vortex cores are offset oppositely along the z-axis, away from the central positions of the vortex supercell. The small-amplitude oscillation around this equilibrium position results in the modulation of diffraction intensity at the fundamental frequencies of the modes, rather than their second harmonics. An analytical model (Supplementary Note 3) further shows that the motion of vortex cores can be parametrized as the vertical displacement ξ of vortex cores (Fig. 3c) away from their equilibrium positions, to which specular reflections such as the 004 peak are particularly sensitive. The analytical model
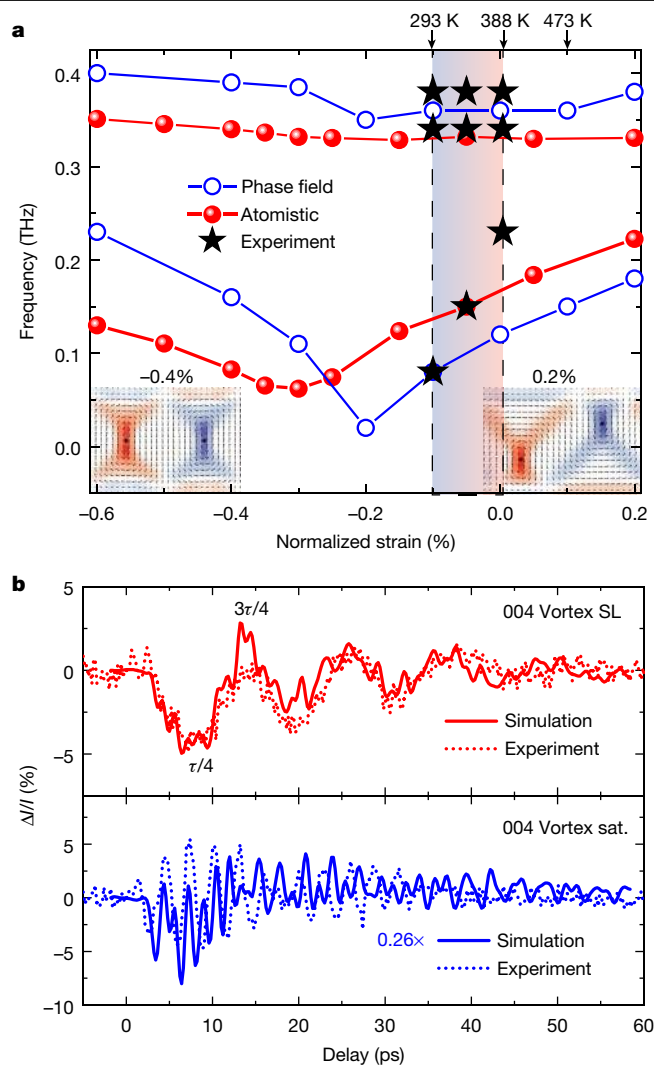
Fig. 4 | Atomistic calculation and dynamical phase-field simulation.
a, Calculated frequencies of collective vortex modes as a function of normalized strain, in comparison with experimental data. The vertical dashed lines indicate the strain at 293 K and 388 K, below the vortex melting temperature of 473 K. The schematics of polar vortex pairs at the bottom show the calculated equilibrium states at −0.4% and 0.2% strain (same key as for Fig. 2d). **b**, Simulated (solid) and measured (dot) normalized change of diffraction intensity of the 004 Bragg peaks as a function of time at 293 K. The simulation results for vortex satellites are scaled by a factor of 0.26 to compare with the amplitude of the measured results. The minimum and maximum intensity changes of the 004 vortex SL peak at delays of τ/4 and 3τ/4 correspond to two configurations shown in Fig. 1b.

also reveals the anharmonic nature of the vortexon (Supplementary Note 3), which opens the route for controlling topological structures via nonlinear phononics[37].

To understand the structural response in the time domain, we used dynamical phase-field simulations to calculate the time-dependent ferroelectric polarization and construct the corresponding atomic positions (Supplementary Note 2, Extended Data Fig. 8). The simulated polarization dynamics captured the eigenmodes obtained from the atomistic calculations (Supplementary Videos 3 and 4). The simulated Bragg-peak intensities as a function of time reproduced the main experimental observations of vortexon modes (Fig. 4b). The subtle difference between the simulated and experimental data for the high-frequency modes is due to the simplifications of the models (Supplementary Note 6). We estimate that ~4% intensity modulation of the 004 vortex

Article

superlattice peak corresponds to maximum lead displacements of ~5 pm (Extended Data Fig. 6e).

To distinguish observed collective dynamics from the conventional superlattice acoustic modes[26,38], we performed a control experiment on the same sample in which we replaced the THz excitation by a 400-nm, 100-fs optical excitation[39]. The intensity modulations of the 004 peak exhibited characteristic frequencies of 0.43 THz and 0.56 THz, corresponding to coherent acoustic waves propagating along the out-of-plane direction at the longitudinal and transverse sound speed in the superlattice, respectively (Supplementary Note 4, Extended Data Fig. 9). Therefore, comparison of the responses to 400-nm and THz excitations unambiguously distinguishes collective modes of polar vortices from the conventional superlattice acoustic modes.

We have experimentally identified a set of collective modes that arise from the unique connectivity of electric polarization and its coupling with the lattice in topological ferroelectric nanostructures. The strain-tunable vortexon mode exhibited collective atomic motions in circular patterns. Combined experimental and theoretical studies revealed their eigenfrequencies and eigenvectors. This level of understanding is critical to exploring new physics and applications of topological structures. For example, the condensation of the vortexon mode at a critical strain could provide a new avenue of phonon engineering in complex oxides. Dynamical phase-field simulation further predicts the tunability of the vortexon mode by external electric field (Extended Data Fig. 6c, d and Supplementary Note 2), offering effective control of the polar-vortex structure at room temperature in nanodevices. These modes have orders of magnitude higher intrinsic frequency and smaller size than their magnetic counterparts, potentially allowing direct electric-field control of their dynamics for high-speed, high-density data processing and storage.

Online content

Any methods, additional references, Nature Research reporting summaries, source data, extended data, supplementary information, acknowledgements, peer review information; details of author contributions and competing interests; and statements of data and code availability are available at https://doi.org/10.1038/s41586-021-03342-4.

1. Naumov, I. I., Bellaiche, L. & Fu, H. Unusual phase transitions in ferroelectric nanodisks and nanorods. *Nature* **432**, 737–740 (2004).
2. Huang, F.-T. & Cheong, S.-W. Aperiodic topological order in the domain configurations of functional materials. *Nat. Rev. Mater.* **2**, 17004 (2017).
3. Choe, S.-B. et al. Vortex core-driven magnetization dynamics. *Science* **304**, 420–422 (2004).
4. Büttner, F. et al. Dynamics and inertia of skyrmionic spin structures. *Nat. Phys.* **11**, 225–228 (2015).
5. Yadav, A. K. et al. Observation of polar vortices in oxide superlattices. *Nature* **530**, 198–201 (2016).
6. Das, S. et al. Observation of room-temperature polar skyrmions. *Nature* **568**, 368–372 (2019).
7. Nagaosa, N. & Tokura, Y. Topological properties and dynamics of magnetic skyrmions. *Nat. Nanotechnol.* **8**, 899–911 (2013).
8. Yadav, A. K. et al. Spatially resolved steady-state negative capacitance. *Nature* **565**, 468–471 (2019).
9. Íñiguez, J., Zubko, P., Luk'yanchuk, I. & Cano, A. Ferroelectric negative capacitance. *Nat. Rev. Mater.* **4**, 243–256 (2019).
10. Stoica, V. A. et al. Optical creation of a supercrystal with three-dimensional nanoscale periodicity. *Nat. Mater.* **18**, 377–383 (2019).
11. Büttner, F., Lemesh, I. & Beach, G. S. D. Theory of isolated magnetic skyrmions: from fundamentals to room temperature applications. *Sci. Rep.* **8**, 4464 (2018).
12. Seidel, J. Domain walls as nanoscale functional elements. *J. Phys. Chem. Lett.* **3**, 2905–2909 (2012).
13. Gu, Z. et al. Resonant domain-wall-enhanced tunable microwave ferroelectrics. *Nature* **560**, 622–627 (2018).
14. Cochard, C., Spielmann, T. & Granzow, T. Dielectric tunability of ferroelectric barium titanate at millimeter-wave frequencies. *Phys. Rev. B* **100**, 184104 (2019).
15. Catalan, G., Seidel, J., Ramesh, R. & Scott, J. F. Domain wall nanoelectronics. *Rev. Mod. Phys.* **84**, 119–156 (2012).
16. Wu, X. et al. Low-energy structural dynamics of ferroelectric domain walls in hexagonal rare-earth manganites. *Sci. Adv.* **3**, e1602371 (2017).
17. Luk'yanchuk, I., Sené, A. & Vinokur, V. M. Electrodynamics of ferroelectric films with negative capacitance. *Phys. Rev. B* **98**, 024107 (2018).
18. Hlinka, J., Paściak, M., Körbel, S. & Marton, P. Terahertz-range polar modes in domain-engineered BiFeO₃. *Phys. Rev. Lett.* **119**, 057604 (2017).
19. Gui, Z. & Bellaiche, L. Terahertz dynamics of ferroelectric vortices from first principles. *Phys. Rev. B* **89**, 064303 (2014).
20. Zhang, Q., Herchig, R. & Ponomareva, I. Nanodynamics of ferroelectric ultrathin films. *Phys. Rev. Lett.* **107**, 177601 (2011).
21. Ogawa, N., Seki, S. & Tokura, Y. Ultrafast optical excitation of magnetic skyrmions. *Sci. Rep.* **5**, 9552 (2015).
22. Hong, Z. et al. Stability of polar vortex lattice in ferroelectric superlattices. *Nano Lett.* **17**, 2246–2252 (2017).
23. Scott, J. F. Soft-mode spectroscopy: experimental studies of structural phase transitions. *Rev. Mod. Phys.* **46**, 83–128 (1974).
24. Li, X. et al. Terahertz field-induced ferroelectricity in quantum paraelectric SrTiO₃. *Science* **364**, 1079–1082 (2019).
25. Nova, T. F., Disa, A. S., Fechner, M. & Cavalleri, A. Metastable ferroelectricity in optically strained SrTiO₃. *Science* **364**, 1075–1079 (2019).
26. Bargheer, M. et al. Coherent atomic motions in a nanostructure studied by femtosecond X-ray diffraction. *Science* **306**, 1771–1773 (2004).
27. Zhu, H. et al. Observation of chiral phonons. *Science* **359**, 579–582 (2018).
28. Qi, T., Shin, Y.-H., Yeh, K.-L., Nelson, K. & Rappe, A. Collective coherent control: synchronization of polarization in ferroelectric PbTiO₃ by shaped THz fields. *Phys. Rev. Lett.* **102**, 247603 (2009).
29. Chen, F. et al. Ultrafast terahertz-field-driven ionic response in ferroelectric BaTiO₃. *Phys. Rev. B* **94**, 180104 (2016).
30. Kozina, M. et al. Terahertz-driven phonon upconversion in SrTiO₃. *Nat. Phys.* **15**, 387–392 (2019).
31. Kubacka, T. et al. Large-amplitude spin dynamics driven by a THz pulse in resonance with an electromagnon. *Science* **343**, 1333–1336 (2014).
32. Damodaran, A. R. et al. Phase coexistence and electric-field control of toroidal order in oxide superlattices. *Nat. Mater.* **16**, 1003–1009 (2017).
33. Li, Q. et al. Quantification of flexoelectricity in PbTiO₃/SrTiO₃ superlattice polar vortices using machine learning and phase-field modeling. *Nat. Commun.* **8**, 1468 (2017).
34. Yang, T., Wang, B., Hu, J.-M. & Chen, L.-Q. Domain dynamics under ultrafast electric-field pulses. *Phys. Rev. Lett.* **124**, 107601 (2020).
35. Trigo, M. et al. Probing unfolded acoustic phonons with X rays. *Phys. Rev. Lett.* **101**, 025505 (2008).
36. Zhang, L. & Niu, Q. Angular momentum of phonons and the Einstein–de Haas effect. *Phys. Rev. Lett.* **112**, 085503 (2014).
37. von Hoegen, A., Mankowsky, R., Fechner, M., Först, M. & Cavalleri, A. Probing the interatomic potential of solids with strong-field nonlinear phononics. *Nature* **555**, 79–82 (2018).
38. Tamura, S., Hurley, D. C. & Wolfe, J. P. Acoustic-phonon propagation in superlattices. *Phys. Rev. B* **38**, 1427–1449 (1988).
39. Daranciang, D. et al. Ultrafast photovoltaic response in ferroelectric nanolayers. *Phys. Rev. Lett.* **108**, 087601 (2012).

Methods

Terahertz or optical-pump, ultrafast X-ray diffraction measurements

The measurements were performed at the X-ray Pump Probe beamline of the Linac Coherent Light Source (LCLS)[40]. The LCLS delivered horizontally polarized X-ray pulses with a pulse duration of 40 fs at a repetition rate of 120 Hz. Hard X-ray pulses at 9.5 keV with 0.05% bandwidth were selected by using a diamond (111) monochromator and focused to ~200 × 200 μm² beam size with beryllium compound refractive lenses. The X-ray beam was attenuated to ~10^9 photons per pulse to avoid sample damage. The sample was mounted on a multi-circle goniometer for both vertical and horizontal scattering geometries. The temperature of the sample stage is controllable within the range of 293 K to 388 K in ambient air with a homebuilt resistive heater. Scattered X-rays were captured shot-by-shot using a high dynamic-range area detector (Jungfrau 1M), positioned at a radial distance of 600–750 mm from the sample.

A Ti:sapphire femtosecond laser system synchronized to the free-electron laser was used to generate 100-fs, 800-nm ultrafast laser pulses with up to 20 mJ pulse energy, which were then converted to single-cycle terahertz pulses by the pulse-front-tilt technique in a LiNbO₃ crystal, as detailed in ref. [41]. The THz pulses were vertically polarized with a maximum peak electric field of ~800 kV cm⁻¹, as calibrated by electro-optic sampling with a GaP crystal. The THz beam was focused on the sample and collinearly aligned with the primary X-ray beam using a 90° off-axis parabolic mirror. In a separate optical pump set-up, 400-nm optical pump pulses were derived by frequency doubling of the 800-nm laser pulses with an incident fluence of 3 mJ cm⁻². The spatiotemporal overlap between optical and X-ray pulses and between optical and THz pulses was achieved using 't0-finder' as detailed in ref. [42].

X-ray scattering patterns around selected diffraction peaks were acquired as a function of delay between the THz/optical pump and X-ray probe pulses with a temporal resolution of ~50 fs, as limited by the pulse duration with correction by the 'timing' tool[40]. A fast measurement scheme was adopted in which the delay was continuously scanned back-and-forth within time delays up to ~40 ps using a mechanical stage; an electronic delay mechanism was applied in combination for longer delays[43]. The raw detector images were grouped into laser on/off data sets (50% laser firing event ratio), normalized against the intensity monitor I_0 (rejecting shots with I_0 lying outside a predefined range) and binned to 100–200 fs temporal slots as needed. Typically, ~500–1,000 effective shots were accumulated for each time sampling data point.

Sample growth and characterization

The (PbTiO₃)₁₆/(SrTiO₃)₁₆ superlattice samples on DSO substrate were fabricated using reflection high-energy electron-diffraction-assisted pulsed laser deposition[5]. Structural characterization and preliminary time-resolved measurements of the samples were carried out using synchrotron-based X-ray diffraction at beamlines 33-ID-C and 7-ID-C of the Advanced Photon Source, respectively. Three-dimensional (3D) reciprocal space maps (RSMs) characterized the structural properties of polar vortex and a_1/a_2 FE structures in the superlattices, which were analysed to determine the strain of both phases as a function of temperature (Extended Data Fig. 7). The FE structures exhibit conventional a_1/a_2 stripe domains with 1.6% smaller out-of-plane lattice constant than the vortex structures, and thus they can be separately probed by X-ray diffraction. These structures have average widths of ~200 nm, and the intermixed regions do not contribute substantially to the measured Bragg diffraction intensity.

Atomistic modelling

The all-atom calculations made use of a parametrization of atomic interactions in the form of the shell model[44]. Therein each atom is represented by a core and a shell, connected by an anharmonic spring, which is designed to mimic atomic polarizability. The potential energy of the system is calculated as a sum of long-range Coulomb interactions between all particles except for cores and shells of the same atom, short-range interactions between shells of oxygen–cation and oxygen–oxygen pairs, and the anharmonic spring interaction for same-atom core–shell pairs. PbTiO₃ (PTO) parameters were taken from ref. [45], whose authors fitted their model to the results of first-principles calculations. This type of PTO potential has been shown to correctly predict vortex structures in a layered material[46]. The SrTiO₃ (STO) parameters were adjusted from ref. [44] to match the atomic charges of PTO, which was necessary to avoid charged interfaces in the layered PTO/STO superstructure. The refined STO parameters are given in Supplementary Table 1. For the Ti and O atoms within an interface atomic layer, averages of the PTO and STO parameters were taken. The programme GULP[47] was used for the structure optimization and lattice dynamics calculations, the details of which are presented in Supplementary Note 1.

Dynamical phase-field calculation

Based on the Landau–Ginzburg–Devonshire (LGD) theory, the PbTiO₃/SrTiO₃ thin-film superlattice system can be described by a free-energy function F integrated over volume V in the following form:

$$F = \int \left(\alpha_{ij}P_iP_j + \alpha_{ijkl}P_iP_jP_kP_l + \alpha_{ijklmn}P_iP_jP_kP_lP_mP_n + \frac{1}{2}g_{ijkl}\frac{\partial P_i}{\partial x_j}\frac{\partial P_k}{\partial x_l} \right.$$
$$\left. + \frac{1}{2}c_{ijkl}\varepsilon_{ij}\varepsilon_{kl} - q_{ijkl}\varepsilon_{ij}P_kP_l - \frac{1}{2}\kappa_b E_iE_i - E_iP_i \right) dV \tag{1}$$

where subscripts i, j, k, l, m and n denote indices (1, 2 and 3) in the Cartesian coordinate; an Einstein summation convention of summations over 1, 2 and 3 for repeating indices is used here and throughout this Article. P_i is one component of the spontaneous polarization vector $\mathbf{P}$, ε_{ij} is total strain, and $E_i = E_i^{in} + E_i^{THz}$ is the total electric field including the effective THz field E_i^{THz} and internal field E_i^{in}; αs are Landau coefficients (up to sixth order for PTO and fourth order for STO), g_{ijkl} are polarization gradient energy coefficients related to the domain wall energy, c_{ijkl} are elastic stiffness tensors, q_{ijkl} are electrostrictive coupling coefficients, and κ_b (isotropic) is the background dielectric permittivity.

We implemented the phase-field model using the finite-element method[33]. The model included three sets of field variables: mechanical displacement $\mathbf{u} = (u_x, u_y, u_z)$, electric potential φ, and polarization vector $\mathbf{P} = (P_x, P_y, P_z)$; other physical quantities in equation (1) can be derived from these variables, for example, $E_x = -\partial\varphi/\partial x$ and $\varepsilon_{xz} = 0.5(\partial u_x/\partial z + \partial u_z/\partial x)$. The Cartesian model coordinates correspond to the pseudocubic crystallographic axes of the samples, as shown in Fig. 1c. For computing efficiency, we studied a thin-slab 3D superlattice model with xyz dimensions of 108 × 0.8 × 152.4 nm³, consisting of eight alternating thin-film layers of 6.4-nm PTO and 6.4-nm STO (approximately 16 unit-cell thickness for each layer) together with a 50-nm substrate layer of DSO. The film was assumed to be fully constrained to the substrate; the displacement of the bottom surface (xy) of DSO was fixed while the top film surface was set mechanically free (that is, $\sigma = 0$). In-plane continuity periodic boundary conditions were imposed for the two opposing pairs of yz and xz surfaces. Short-circuit electrical boundary conditions (that is, $\varphi = 0$) were applied for both top and bottom film surfaces. The mechanical strain state of the entire system was calculated with reference to the cubic-phase PTO, assuming the lattice constants of cubic PTO (3.955 Å), STO (3.905 Å) and DSO (3.951 Å and 3.945 Å along the x and y axes, respectively). The model geometry was discretized into a mesh of 0.8-nm cube elements with the quadratic Lagrange shape function.

The spatiotemporal dynamics of the superlattice system is governed by the following set of coupled equations of motion[34]:

Article

$$\mu \ddot{P}_i + \gamma \dot{P}_i = -\delta F / \delta P_i \tag{2}$$

$$\rho \ddot{u}_i + \beta \rho \dot{u}_i = -\delta F / \delta u_i \tag{3}$$

$$0 = \delta F / \delta \varphi \tag{4}$$

in which μ is the effective polarization mass density, γ is the polarization damping coefficient, ρ is the mass density and β is the elastic damping coefficient. Equation (2) is a second-order time-dependent LGD equation that explicitly controls the dynamics of the polarization order parameter, while equation (3) explicitly controls the elastodynamics (yet they are coupled via the electrostriction effect). In formulating equation (4), we imply that there are no complex electrodynamics associated with electron/hole carrier transport since the intrinsic carrier concentration in the system can be neglected, and low-energy THz excitation (versus 400-nm optical pump) does not populate free carriers in this system. Note that equation (3) governs both the superlattice film and substrate layers whereas equations (2) and (4) are defined only for the film layers.

Typically, we first nullified the mass inertial effects by setting both μ and ρ as zero and generated a quasi-steady state vortex configuration from an initial random state consisting of small polarization values ($<0.001 P_0$, $P_0 = 0.7\,\mathrm{C\,m^{-2}}$). We then turned on the mass parameters and equilibrated the model for ~40–100 ps before executing excitation runs. To simulate the THz excitation, we added a time-dependent electric-field pulse $E_i^{\mathrm{THz}}(t)$ to the internal electric field which had a realistic THz waveform as measured from the electro-optical sampling, and we combined $x/y/z$ components according to a specific measurement condition. The peak amplitude of the applied electric field was 100–200 kV cm^{-1}, taking into account the dielectric screening by the PTO/STO film due to the background permittivity, and was finely tuned to match the measured X-ray scattering signals. The generalized-alpha time stepping method was adopted to solve equations (2)–(4), where the maximum step was limited to 0.1 ps to eliminate high-frequency numerical errors. Further details of the dynamical phase-field calculation and the simulation of time-dependent X-ray diffraction intensity can be found in Supplementary Note 2. The response spectra, which display the time-dependent changes of averaged polarization P^2 in Fig. 1a, were calculated upon THz excitation with a peak electric field of $1 \times 10^7\,\mathrm{V\,m^{-1}}$ along the x-axis using the parameters listed in Supplementary Table 2.

Data availability

The data that support the findings of this study are available from the corresponding author upon request.

Code availability

The codes that support the findings of this study are available from the corresponding author upon request.

40. Chollet, M. et al. The X-ray Pump–Probe instrument at the Linac Coherent Light Source. *J. Synchrotron Radiat.* **22**, 503–507 (2015).
41. Kozina, M. et al. Ultrafast X-ray diffraction probe of terahertz field-driven soft mode dynamics in SrTiO$_3$. *Struct. Dyn.* **4**, 054301 (2017).
42. Sato, T. et al. A simple instrument to find spatiotemporal overlap of optical/X-ray light at free-electron lasers. *J. Synchrotron Radiat.* **26**, 647–652 (2019).
43. Glownia, J. M. et al. Pump–probe experimental methodology at the Linac Coherent Light Source. *J. Synchrotron Radiat.* **26**, 685–691 (2019).
44. Sepliarsky, M., Asthagiri, A., Phillpot, S. R., Stachiotti, M. G. & Migoni, R. L. Atomic-level simulation of ferroelectricity in oxide materials. *Curr. Opin. Solid State Mater. Sci.* **9**, 107–113 (2005).
45. Sepliarsky, M. & Cohen, R. E. First-principles based atomistic modeling of phase stability in PMN–xPT. *J. Phys. Condens. Matter* **23**, 435902 (2011).
46. Stachiotti, M. G. & Sepliarsky, M. Toroidal ferroelectricity in PbTiO$_3$ nanoparticles. *Phys. Rev. Lett.* **106**, 137601 (2011).
47. Gale, J. D. & Rohl, A. L. The General Utility Lattice Program (GULP). *Mol. Simul.* **29**, 291–341 (2003).

Author contributions Q.L., V.A.S., Y.Y., M.R.M., S.P., H.J.L., Y.A., S.D.M., T.S., M.C.H., M.C., M.E.K., S.N., D.Z., A.M.L., P.G.E., V.G., J.W.F. and H.W. performed the experiment at the Linac Coherent Light Source. Y.Z., V.A.S., D.A.W. and H.W. performed preliminary experiments at the Advanced Photon Source. M.P. and J.H. performed atomistic modelling. Q.L., C.D., T.Y. and L.-Q.C. performed phase-field simulation. T.Y., L.-Q.C. and J.H. developed the analytical model. S.D., M.R.M., A.K.Y., L.W.M. and R.R. prepared the samples. S.Y. and C.K. performed THz spectroscopy measurements. Q.L. and H.W. wrote the manuscript with input from all authors. H.W. conceived and supervised the project.
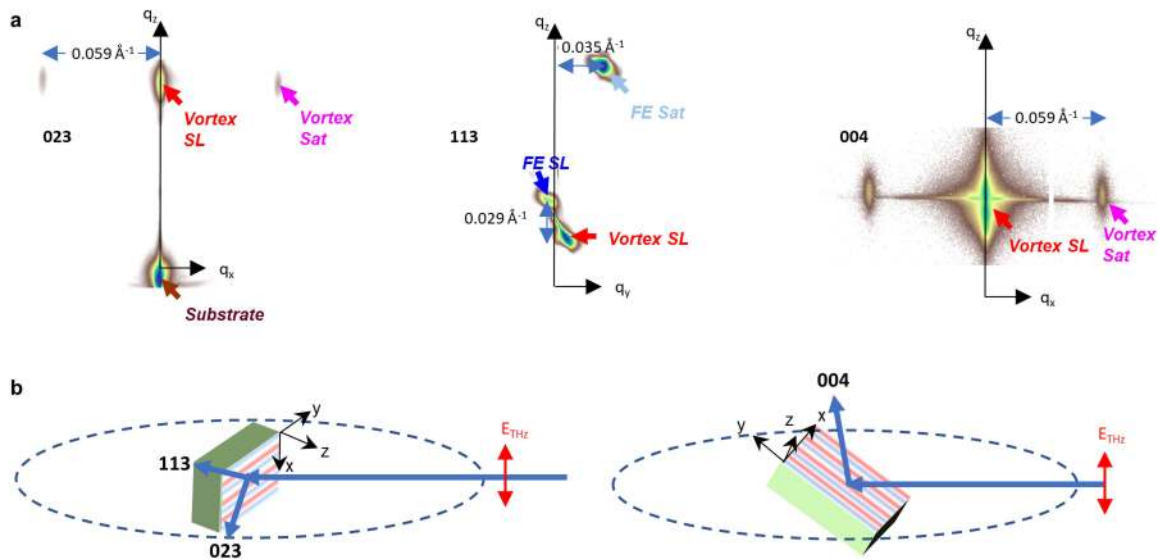
**Extended Data Fig. 1 | Diffraction patterns of probed Bragg peaks and the corresponding diffraction geometry. a**, Diffraction patterns of 023, 113 and 004 peaks in logarithmic scale as recorded by a two-dimensional X-ray area detector. The projected *q*-axis labels indicate the approximate directions in reciprocal space. **b**, Schematics of diffraction geometry for probing the 023, 113 and 004 peaks. The dashed circle represents the horizontal plane. The red and blue stripes represent vortex structure with opposite vorticities. The THz field is polarized vertically.

Article
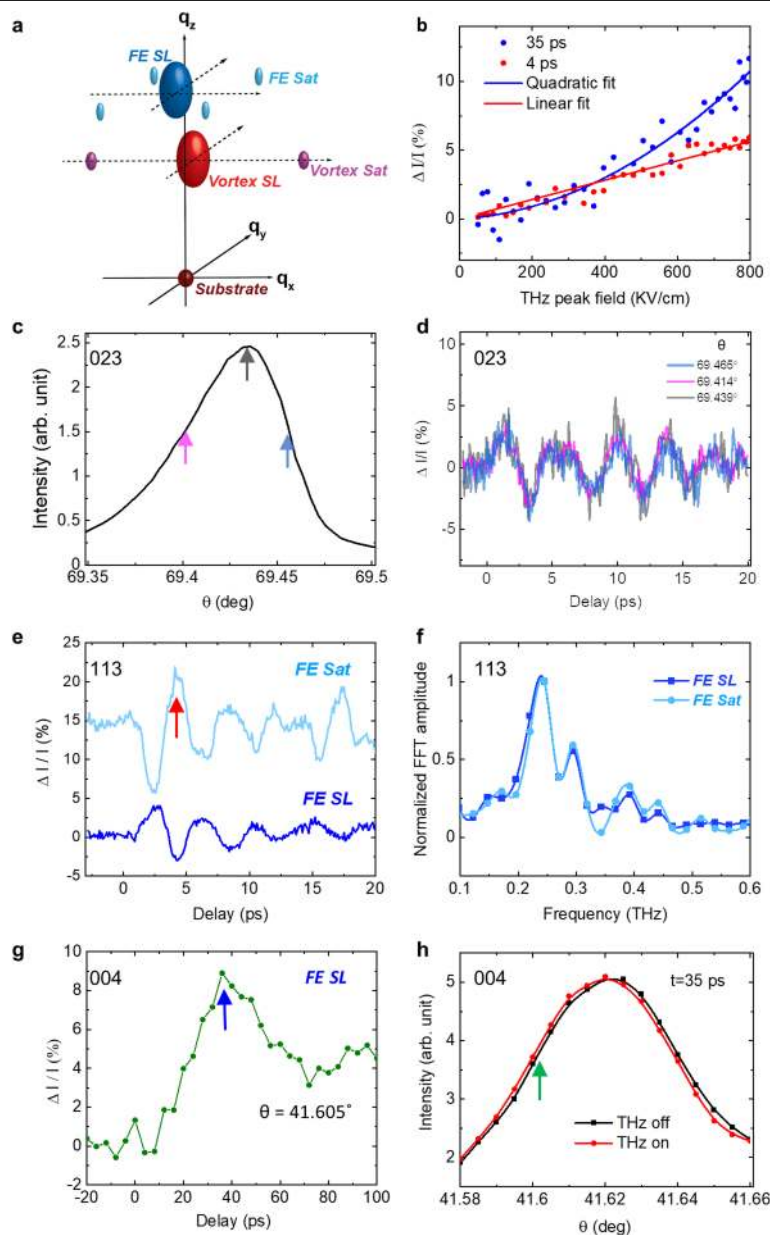
Extended Data Fig. 2 | The response of the FE (a_1/a_2) structure upon THz field excitation. a, 3D schematic of diffraction peaks of the film around the 023 or 113 substrate peaks in reciprocal space. The dashed arrows indicate the reciprocal axes through the centres of the FE or vortex SL peaks that are offset along the q_y-axis owing to the lattice constant difference along the y-axis. Only two SL and their satellite peaks are shown for simplicity. **b**, Normalized change of diffraction intensity of the 113 FE satellite peak (red curve) measured at the delay of 4 ps indicated by the red arrow in **e**, and normalized change of diffraction intensity of the 004 FE SL peak (blue curve) measured at the delay of 35 ps indicated by the blue arrow in **g**, as a function of the applied THz peak field. Lines are linear and quadratic fits to the measured data, in agreement with the field-driven structure factor modulation and the THz-induced Bragg

peak shift (heating), respectively. **c**, Rocking curve of 023 FE SL peak. **d**, Normalized change of diffraction intensity as a function of delay measured at various incident angles indicated by the magenta, grey and blue arrows in **c**. **e**, Normalized change of diffraction intensity of the 113 FE SL peak and its satellites as a function of delay. The curves are vertically offset for clarity. **f**, Fourier spectra of **e**. **g**, Normalized change of diffraction intensity as a function of delay measured at the lower-angle side of the 004 FE SL peaks, indicated by the green arrow in **h**. **h**, Rocking curves of 004 FE SL peak measured at the delay of 35 ps with and without THz excitation. The peak shift shows a strain of 2.5×10^{-5}, corresponding to a 2 K temperature rise as calibrated by the temperature-dependent X-ray diffraction measurements shown in Extended Data Fig. 7b.
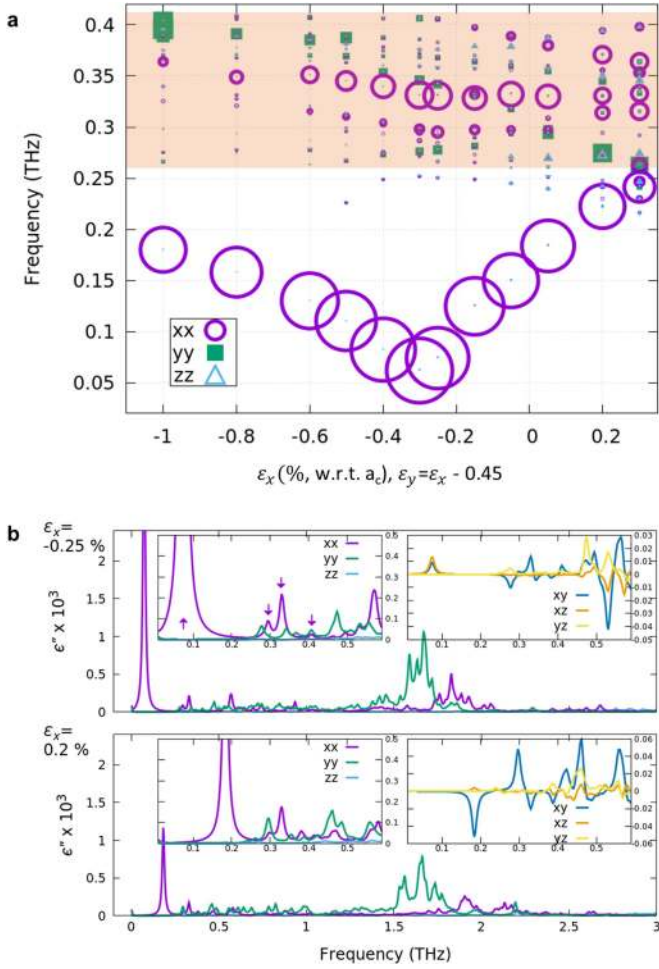
Extended Data Fig. 3 | The dielectric properties of vortex structures as a function of strain and frequency from atomistic calculations.
a, Frequency–strain diagram with the diagonal oscillator strength (S_{ii}) of each mode reflected in the size of the markers (the area is proportional to $\log(S_{ii}+1\,THz^2))$, where i represents x, y or z. The dielectric strength of the mth mode ($\Delta\epsilon_{ii,m}$) is directly related to the oscillator strength via $\Delta\epsilon_{ii,m}=S_{ii,m}/\omega_m^2$, where ω_m is the mode's frequency. The 15 lowest-frequency modes are considered; the zz signal is multiplied 5 times for better visibility. The orange area indicates the high-frequency regime. **b**, Frequency-dependent permittivity for two different strain values, $\epsilon_x = -0.25\%$ and 0.2%. The imaginary part is presented in the main plots, while the left-hand insets show diagonal components $\epsilon''_{xx}, \epsilon''_{yy}, \epsilon''_{zz}$ and the right-hand insets present off-diagonal spectra $\epsilon''_{xy}, \epsilon''_{xz}, \epsilon''_{yz}$. The arrows indicate modes that are analysed in the Extended Data Fig. 4. All dielectric properties are calculated for the PTO layer only.
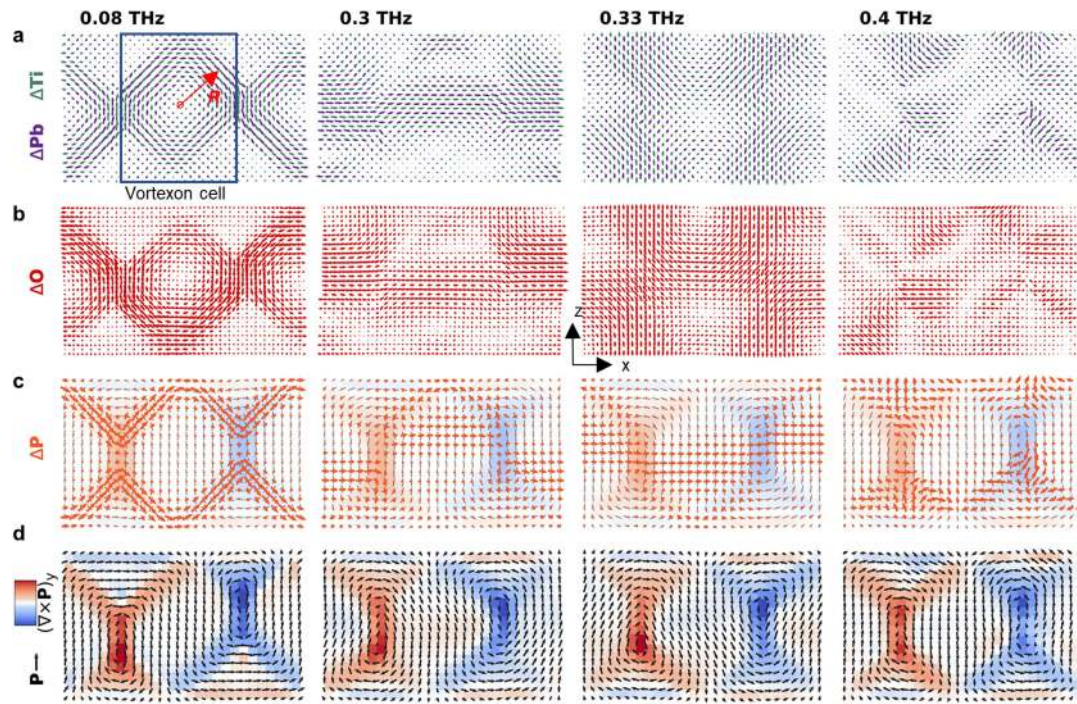
Extended Data Fig. 4 | Decomposition of selected modes with strain $\varepsilon_x = -0.25\%$ in the atomistic model. The modes are characterized by the highest oscillator strengths in the x-direction (below the frequency of 0.41 THz, marked by the arrows in Extended Data Fig. 3b), and the first two of them are also described in the main text. **a**–**d**, Each column contains microscopic configurations at $t = \tau/4$ of (**a**) Pb and Ti displacements; (**b**) O displacements of the mode's eigenvectors; (**c**) change in polarization caused by these atomic displacements (overlaid on a $\nabla \times \mathbf{P}$ map of the equilibrium structure);

(**d**) polarization patterns and the respective $\nabla \times \mathbf{P}$ map of a structure subjected to the mode's perturbation. The origin **O** and vector **R** in **a** are related to the calculation of the angular momentum of the vortexon in the boxed region detailed in Supplementary Note 1B. The displacement vectors are scaled arbitrarily, while perturbed (**P**) configurations are calculated for maximum ionic displacements of 30 pm. We note that there are additional modes with the y-component of the oscillator strength that contribute to the diversity of the collective dynamics in the frequency range 0.3–0.4 THz.
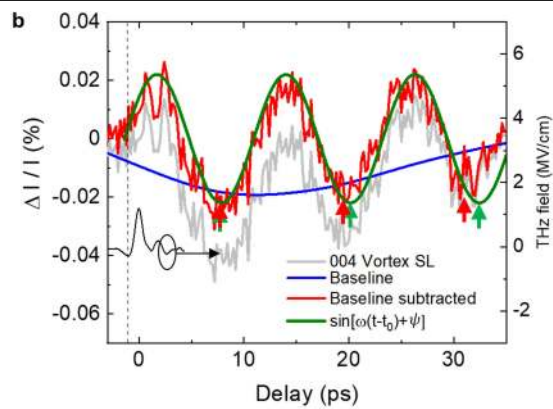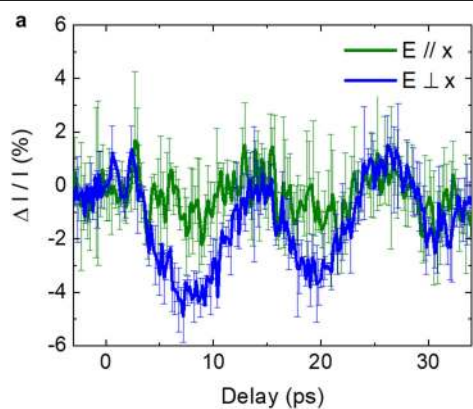
Extended Data Fig. 5 | Polarization dependent response and analysis of the vortexon mode. a, Normalized change of diffraction intensity of 004 vortex Bragg peak as a function of time when the THz field is applied parallel to and perpendicular to the crystalline x-axis. **b**, Baseline-subtracted normalized change of diffraction intensity of the 004 vortex superlattice peak (red curve) as a function delay. Raw data shown in grey are from Fig. 4b. The green curve shows a sinusoidal wave (see Supplementary Note 5), with its minima (green arrows) deviating from the data (red arrows) at later times. The vertical dashed line indicates the time when the THz field turns on.
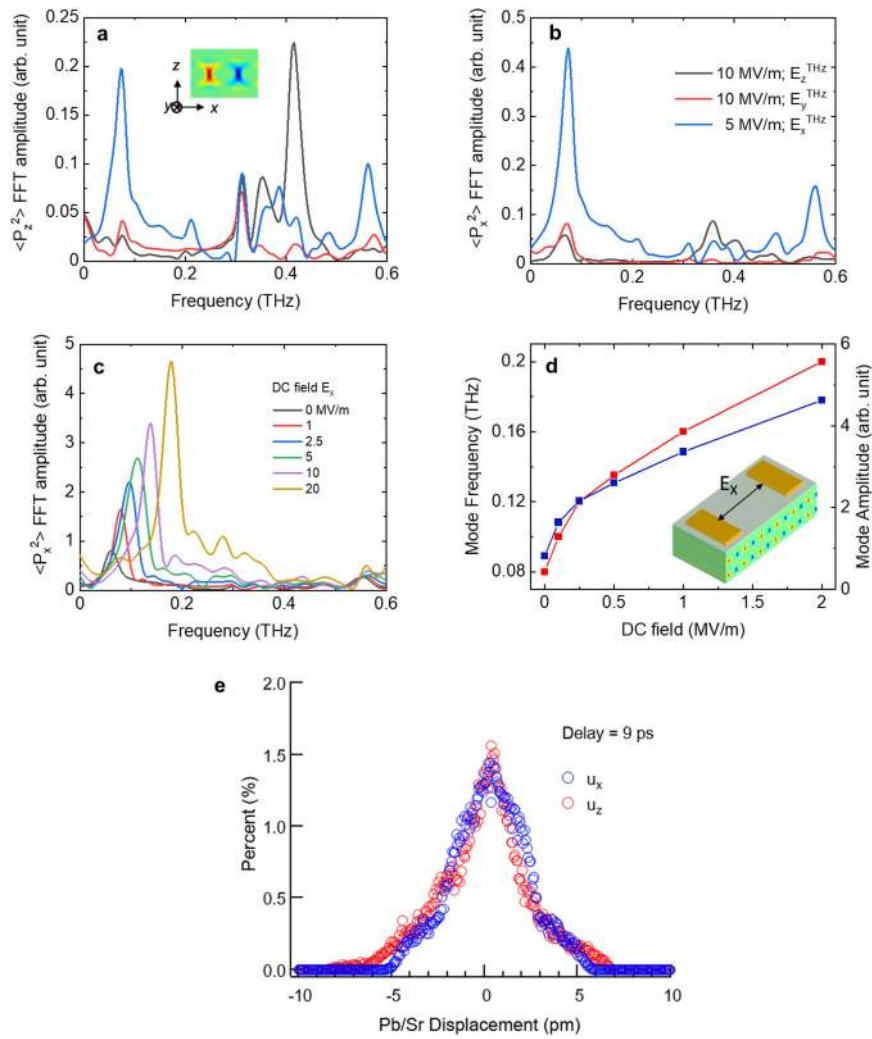
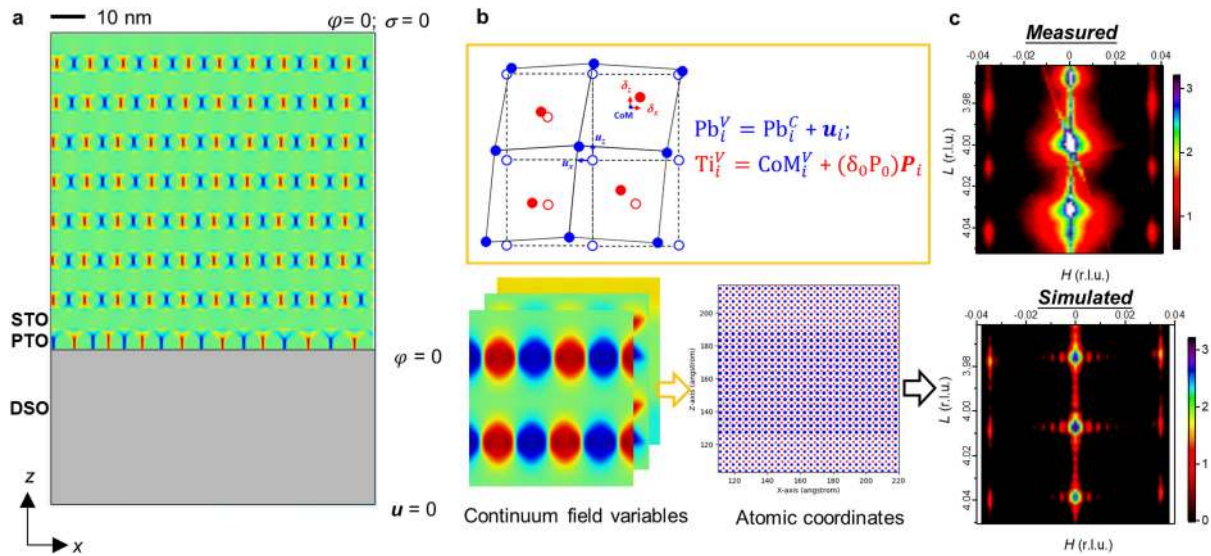**Extended Data Fig. 6 | Dynamical phase-field simulation results.**
a, **b**, Fourier transform of the simulated polarization dynamics, which is represented by spatially averaged (**a**) P_z^2 and (**b**) P_x^2 in the simulation box on application of the THz-field pulse aligned along the x-, y- or z-axis. **c**, Calculated frequency spectra of P_x^2 with various values of the direct-current (DC) electric field along the x-axis. **d**, Frequency and amplitude of the vortexon mode as a function of the applied electric field (E_x). Such an in-plane electric field can be applied using a pair of coplanar electrodes, as schematically shown in the inset to **d**. **e**, Histograms of the Pb and Sr ionic displacement **u** away from its equilibrium positions along the x- and z-axes, corresponding to the maximum diffraction intensity change of 4% of 004 SL peak at a delay of 9 ps in the simulation.
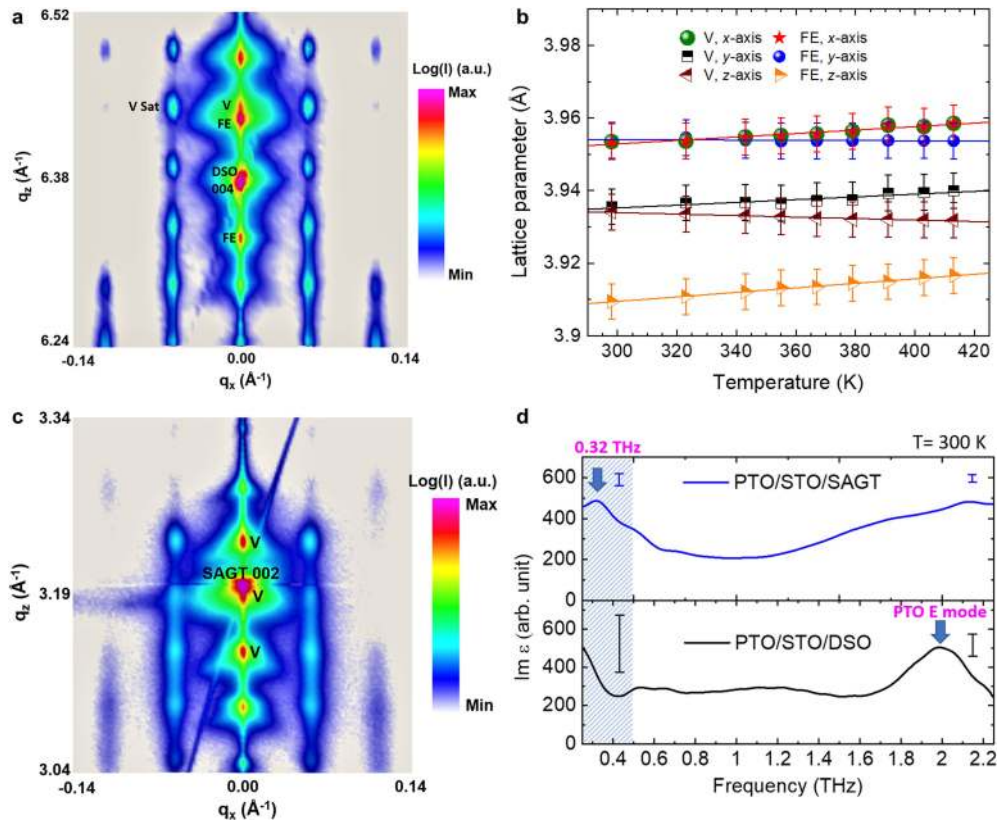
Extended Data Fig. 7 | Equilibrium characterizations of $(PbTiO_3)_{16}/(SrTiO_3)_{16}$ superlattice. a, Room-temperature RSM of the superlattice grown on DSO substrate, cutting through the substrate specular 004 peak, which shows vortex (V) and FE superlattice diffraction peaks in the q_x–q_z plane. The satellites (V Sat) due to the in-plane vortex ordering appear along the q_x direction around the corresponding superlattice (V) peaks. **b**, The measured average lattice parameters with linear fits for the vortex and FE structures as a function of temperature. The error bars represent systematic errors of the measurement.

c, Room-temperature RSM of the superlattice grown on $Sr_2Al_{0.3}Ga_{0.7}TaO_6$ (SAGT) substrate, cutting through the substrate specular 002 peak, which shows the vortex SL diffraction peaks and satellites. **d**, Room-temperature imaginary dielectric constant extracted from the THz time-domain absorption spectroscopy measurements of superlattices grown on DSO and SAGT substrates. The error bars represent the estimated experimental errors in the frequency ranges of the shaded and unshaded regimes.

Extended Data Fig. 8 | X-ray diffraction simulations based on dynamical phase-field modelling. a, Model geometry of the PTO/STO superlattice film and the DSO substrate. The colour scale denotes the vorticity of the polarization vectors. The boundary conditions (Methods) are marked on the right. **b**, Schematics for the method used to map the phase-field modelling output to atomistic configurations, based on which kinematic X-ray scattering intensities are calculated (Supplementary Note 2). CoM, center of mass; V and C denote the vortex and cubic phases of $PbTiO_3$, respectively. **c**, Measured and simulated $H0L$-cut (along the q_x–q_z plane in reciprocal lattice units (r.l.u.)) RSMs near the 004 reflection with the intensity shown on a logarithmic colour scale. The fringes in the simulated RSM are due to the finite lateral size of the simulation box.
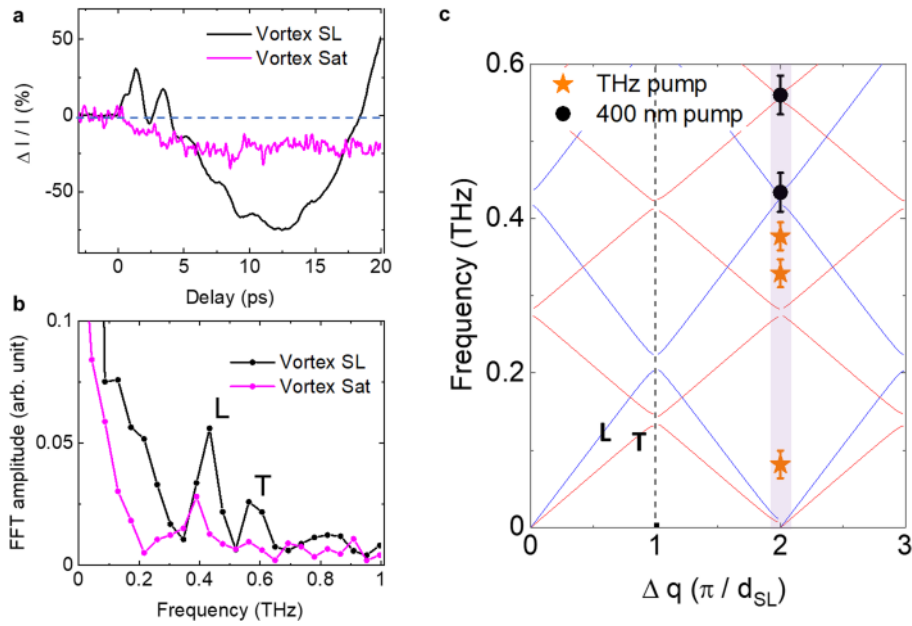
Extended Data Fig. 9 | Structural dynamics excited by 400-nm optical pulses. a, Normalized changes of 004-vortex peak intensity as a function delay. **b**, Fourier spectra of **a**. L and T represent the acoustic waves that travel along the out-of-plane direction with longitudinal and transverse sound speeds, respectively. **c**, Calculated phonon dispersion curves. The vertical dashed line indicates the boundary of the folded Brillouin zones. The shaded region corresponds to the scattering vectors probed in the experiment. The solid circles show the measured modes upon 400-nm excitation, while the stars show the measured modes upon THz excitation. The error bars show the full-width at half-maximum of the peaks in the Fourier spectra. d_{SL}, superlattice periodicity.